

QUENCH AND FIELD DEPENDENT SURFACE RESISTANCE STUDIES USING A SINGLE CELL CAVITY WITH ARTIFICIAL PITS *

Y. Xie † and M. Liepe

Cornell Laboratory for Accelerator-Based Sciences and Education (CLASSE),
Cornell University, Ithaca, NY 14853, USA

Abstract

Surface defects such as pits have been identified as some of the main sources of limitations of srf cavity performance. A single cell cavity was made with 30 artificial pits in the high magnetic field region to gain new insight in how pits limit the cavity performance. The test of the pit cavity showed clear evidence that the edges of two of the largest radius pits transitioned into the normal conducting state at field just below the quench field of the cavity, and that the quench was indeed induced by these two pits. Insights about quench and non-linear rf resistances will be presented.

INTRODUCTION

Pit-like structures on the niobium surface of srf cavities have been shown to cause thermal breakdown under certain conditions [1]. Thus we need to understand better how pits cause quench and what the relevant parameters are. This can be done experientially and by simulating pits.

However, the field at which quench is caused by a pit defect varies significantly from pit to pit, and frequently, pits do not cause quench up to the maximum field obtained. Previous thermal feedback models treat pits as normal conducting disks assuming the entire pit area is normal conducting starting from low field [1]. Yet real pit-like defects observed in srf cavities have a complex 3-dimensional shape which can not be simply treated as a all normal conducting disk. Recent electromagnetic simulations show that the magnetic field enhancement (MFE) effect is present at the sharp edge or corner of a pit. It was calculated that a pit MFE factor β shows a $(r/R)^{-1/3}$ dependence, where r is the radius of the pit edge and R is the radius of the pit [2]. Therefore a more accurate ring-type defect model in which only pit edges get normal conducting above a certain magnetic field level was developed [3].

Previous experimental studies depended on random data sets collected from pits occasionally found on srf cavities. In order to systematically study the nature of pit-induced quench, a single-cell niobium srf cavity with many artificially drilled pits with different sizes was prepared and tested. Thermometers attached outside the cavity pit locations recorded heating signals as function of the rf magnetic field level.

PITS CAVITY DESIGN AND FABRICATION

A single cell cavity with artificial pits is an ideal tool to investigate pits induced cavity quench and even the high field Q-slope phenomena. The Magnetic field enhancement (MFE) factor h at the pit edges depends only on pit radius R and edge radius r if the pit depth is several times larger than its radius (see later for a detailed discussion of the magnetic field enhancement by pits).

A single cell 1.3 GHz niobium cavity of the Cornell ERL center cell shape was fabricated. Prior to joining the two halves of the cavity by electron-beam welding, 30 pits of various radii were drilled into the inside niobium wall in the high magnetic field region of the cavity, each 1.5 mm deep, which is half of the wall thickness of the cavity. Fig. 1 shows the fabricated half cup with different sizes of pits.



Figure 1: Half cup of the pit cavity after drilling of the pits.

In order to obtain different MFE factors of the artificial pits, pit of 5 different radii R were drilled perpendicular to the cavity wall, with six copies of each size. After drilling the pits and after final electron beam welding of the equator to join the two cavity halves, a heavy BCP of about 120 μm was applied to the pits cavity. This BCP process determined the pits edge radius r along with the different drill sizes used. The parameters of the pits are summarized in Table 1.

In order to use the Cornell single-cell temperature mapping system to record the rf heating from the pits, the pit position pattern is matched to thermometry sensor positions (Fig. 2). In the pit cavity, pits are spaced by 18.95 deg, so that a pit is located under a specific temperature sensor on every other board. The single-cell T-map has 38 boards in the azimuthal direction, thus the boards are spaced by 9.47 deg. For example, pit positions 1 to 3 have

* Work supported by NSF and Alfred P. Sloan Foundation.

† yx39@cornell.edu, now at Euclid Techlabs LLC.

Table 1: Pit Parameters for the Pits Cavity

Total number of pits	30
Pits radii	200, 300, 400, 600, 750 μm
Pits edge radii	initially unknown
Pits depth	1.5 mm
Pits position	1 inch from the cavity equator

a radius of 200 μm and pit positions 4 to 6 have a radius of 300 μm . Note that pits are located symmetric to the equator, so that at every given angular position there are two pits, one above and one below the equator. Since all pits are located at the same distance from the equator, they all will see the same local magnetic field, not taking into account any differences in magnetic field enhancement by the pits.

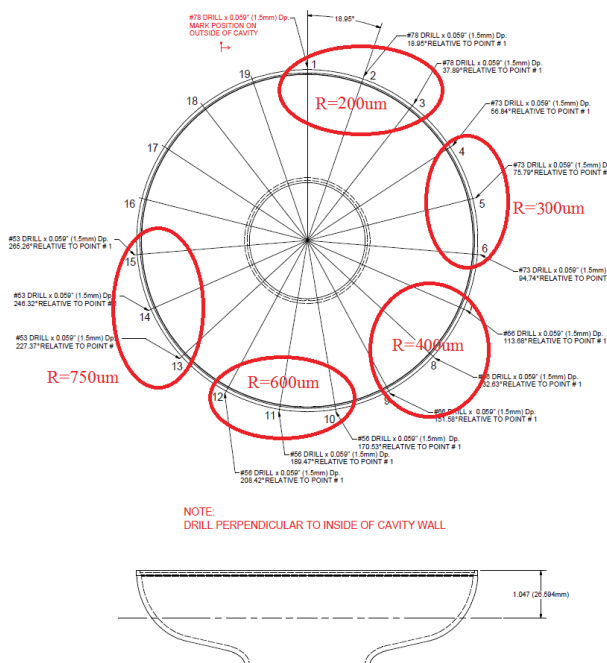


Figure 2: Distribution of pits along the inner surface of the cavity.

PIT CAVITY EXPERIMENTAL RESULTS

After fabrication, the cavity with the 30 drilled pits of various radii received a 120 μm BCP, was high pressure water rinsed and dried for assembly to the test insert in a class 10 clean room, and received a final 120 C in-situ bake. In the following sections, we present the results from the rf test of the cavity, and show temperature maps taken by a large scale temperature mapping system mounted to the outside of the cavity. Also, we show results from a laser confocal microscope inspection of molds taken from the pits in the cavity after the rf test. The microscope data gives

05 Cavity performance limiting mechanisms

F. Basic R&D bulk Nb - High performances

important pit shape information, especially the radius r of the edge of the pits. The edge radius strongly impacts the magnetic field enhancement at the edge of the pits, and thus needs to be measured after the final BCP of the cavity to reflect the situation present during test of the cavity.

RF Test Results

Results of the rf test at 1.6 K are shown in Fig. 3. The cavity quenched at a maximum surface magnetic field of 550 Oe which corresponds to an accelerating field of 11 MV/m. It should be noted that the maximum surface magnetic field quoted here and Fig. 4 does not include the local magnetic field enhancement by the pit. At the pit edge, the local magnetic field is significantly higher, as discussed later.

Before the quench, a mild Q-drop effect appeared above 300 Oe. There is a sudden drop in Q_0 at about 520 Oe, followed by a strong Q-slope. As we will discuss later, at this field the local, enhanced magnetic field at the first pit edge reaches the critical magnetic field and the edge starts to transition into the normal conducting state, thereby decreasing the cavity's quality factor. No x-rays were registered and thus no field emission was present during the test. The pits cavity was also tested at different tempera-

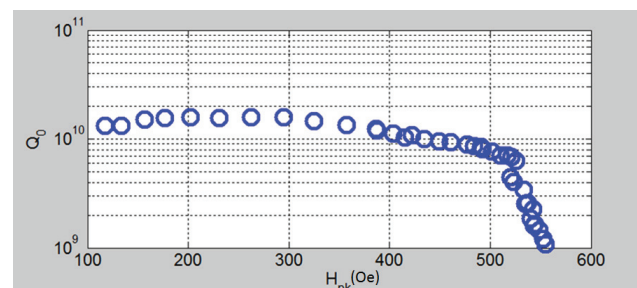


Figure 3: The pits cavity quality factor Q_0 versus the peak surface magnetic field H_{pk} at 1.6 K. The uncertainty in the measured field is $\pm 10\%$ and $\pm 20\%$ in Q_0 . The surface magnetic field on the horizontal axis is the peak surface field of the cavity, not taking into account the local field enhancement by the pits.

tures as 2.0 K, 3.0 K and 4.2 K. The results are summarized in Fig. 4. The pits cavity quenches around the same peak surface magnetic field of 550 Oe corresponding to accelerating field of 11 MV/m. The quality factor differences between 1.6 K, 2.0 K, 3.0 K and 4.2 K are due to the temperature dependence of the BCS resistance.

Temperature Map Results

The single-cell T-map system was used to measure the rf heating at the pits locations as function of magnetic field during the entire cavity rf test. Before temperature maps of all the thermometers were taken, three calibrated Cernox thermometers placed inside the helium bath were used to calibrate the T-map from 4.2 K to 1.6 K at an interval of 0.1 K. The calibration process was done along with slow

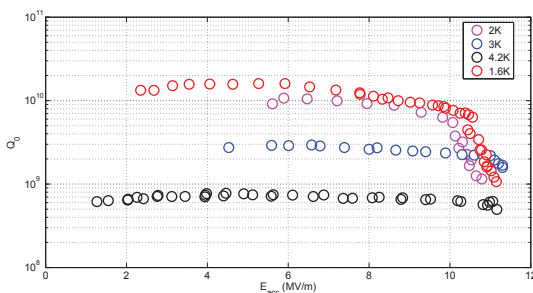


Figure 4: The pit cavity quality factor Q_0 versus the accelerating field E_{acc} at different temperatures. A E_{acc} of 11 MV/m corresponding to maximum surface magnetic field H_{pk} of 550 Oe. The uncertainty in the measured field is $\pm 10\%$ and $\pm 20\%$ in Q_0 .

helium cool down from 4.2 K to 1.6 K. Since the resistive element of the thermometers is carbon, which is a semiconductor, one would expects an exponential decrease of resistance with increasing temperature. After calibration, the temperature dependence of the thermometer resistance data was fitted by a polynomial function of third order,

$$\frac{1}{T} = a_n + b x_n + c x_n^2 + d x_n^3; \quad x_n = \ln R_n \quad (1)$$

where T is the bath temperature measured by the Cernox thermometers, R_n is the resistance of carbon thermometer n , and a_n, b_n, c_n and d_n are fit parameters. Fig. 5 shows an example of a calibration curve for one of the temperature sensors taken during the calibration of the T-map for the pit cavity test. The voltage over the resistor is plotted instead of the resistance itself, because a fixed current source was used to drive the T-map thermometers, and the voltage over the resistors is measured by the data acquisition system. After calibration, temperature maps were taken at different fields up to the quench field of the cavity. As an example, Fig. 6 shows one T-map taken at the cavity maximum surface magnetic field of 350 Oe. The artificial pits are located at the following positions of the T-map:

- Resistor number 6 and 12;
- Board number (2,4,6); (8,10,12); (14,16,18); (20,22,24); (26,28,30);

Here a number scheme was introduced for all 30 pits. For example, pit (2,6) (Board number 2, Resistor number 6) was named pit #1. Tab. 2 shows the detailed pit number scheme.

As pits cavity maximum surface magnetic field increases, the heating pattern keeps nearly the same and the heating get stronger as can be seen in Fig. 7, which shows the T-map taken around 500 Oe.

The ratio between the field at the positions of the pits and the maximum surface magnetic field of the cavity, not taking into account the magnetic field enhancement by the pits, is 0.98 as found by CLANS calculations [4].

From this T-map data, we can conclude that:

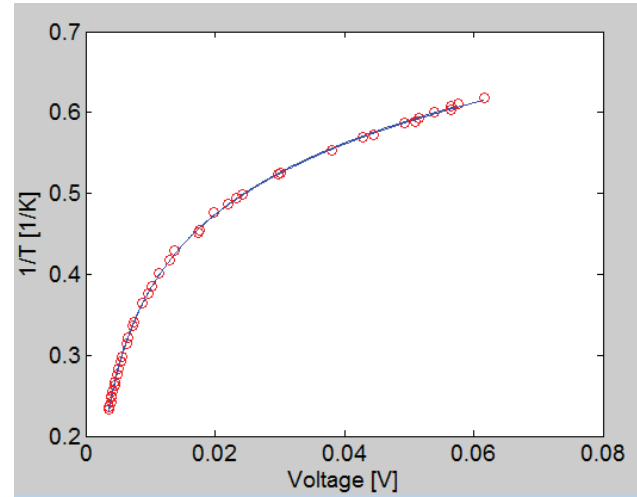


Figure 5: Calibration data obtained for one of the temperature sensors of the T-map system during the calibration of the temperature mapping system during the test of the pit cavity. Red circles: data points. Blue curve: polynomial fit according to Eqn. 1.

Table 2: The Number Scheme of the 30 Artificial Pits

Board #	Resistor #	Pit #	Board #	Resistor #	Pit #
2	6	#1	16	12	#16
2	12	#2	18	12	#17
4	6	#3	18	12	#18
4	12	#4	20	6	#19
6	6	#5	20	12	#20
6	12	#6	22	6	#21
8	6	#7	22	12	#22
8	12	#8	24	6	#23
10	6	#9	24	12	#24
10	12	#10	26	6	#25
12	6	#11	26	12	#26
12	12	#12	28	6	#27
14	6	#13	28	12	#28
14	12	#14	30	6	#29
16	6	#15	30	12	#30

- T-map heating pattern does correlate well with the pattern of the actual artificial pit positions on the inner cavity surface.
- Smaller diameter pits show smaller heating and larger diameter pits show larger heating in general. This is in agreement with the simple magnetic field enhancement model, which predicts that the local magnetic field enhancement at the edges of the pits scales with the radius R of the pits according to $R^{1/3}$ [2], assuming that the edges of all pits have the same sharpness. Accordingly, larger pits will have higher local fields, thus larger rf heating.

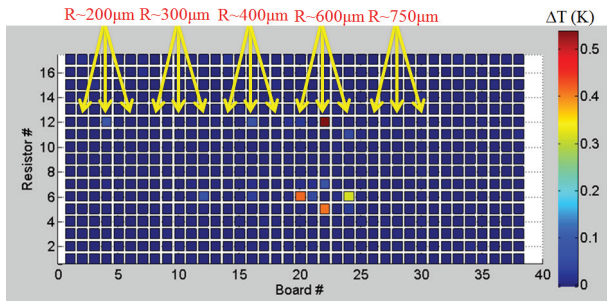


Figure 6: T-map taken at H_{pk} of 350 Oe. Plotted here are ΔT between rf on and off. The uncertainty in ΔT is ± 1 mK. Note that the T-map data shows good correlation between the heating pattern and the position of the pits. The row of resistors #9 is at the equator of the cavity. The 38 boards are spaced equally around the cavity.

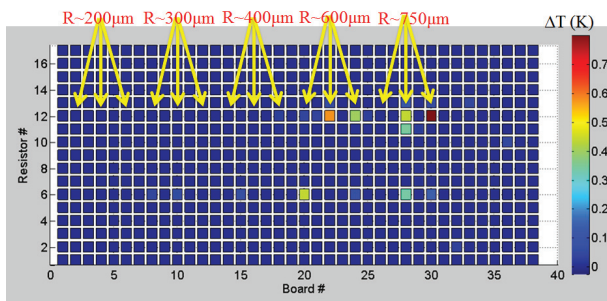


Figure 7: T-map taken at H_{pk} of 500 Oe. Plotted here are ΔT between rf on and off. The uncertainty in ΔT is ± 1 mK. Note the heating gets larger as compared to the heating at 350 Oe shown in Fig. 6. The row of resistors #9 is at the equator of the cavity. The 38 boards are spaced equally around the cavity.

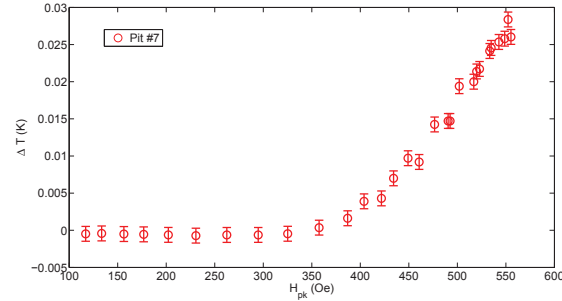


Figure 9: The heating of pit #7 with radius $R = 300 \mu\text{m}$ versus surface magnetic field. The heating signals from other 5 pits with radius $R = 300 \mu\text{m}$ are missing because of non-functional temperature sensors. The surface magnetic field on the horizontal axis is the peak surface field of the cavity, not taking into account the local field enhancement by the pits.

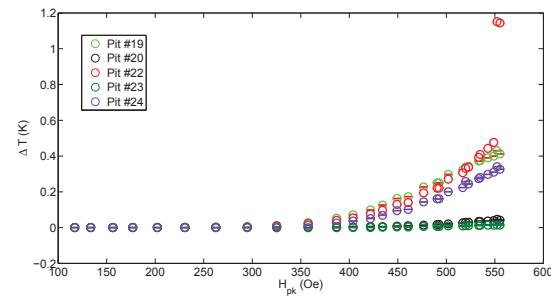


Figure 10: The heating of pit #19, #20, #22, #23 and #24 with radius $R = 600 \mu\text{m}$ versus surface magnetic field. The heating signal of pit #21 is missing because of a non-functional temperature sensor. The surface magnetic field on the horizontal axis is the peak surface field of the cavity, not taking into account the local field enhancement by the pits.

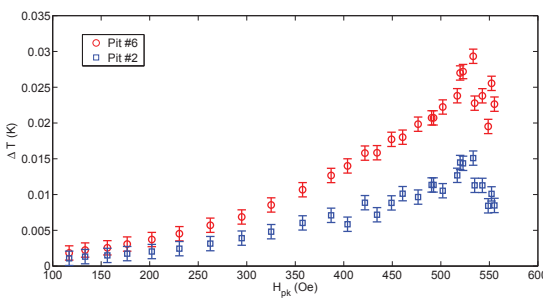


Figure 8: The heating of pit #2 and #6 with radius $R = 200 \mu\text{m}$ versus surface magnetic field. The heating signals from the other 4 pits with radius $R = 200 \mu\text{m}$ are missing because of non-functional temperature sensors. The surface magnetic field on the horizontal axis is the peak surface field of the cavity, not taking into account the local field enhancement by the pits.

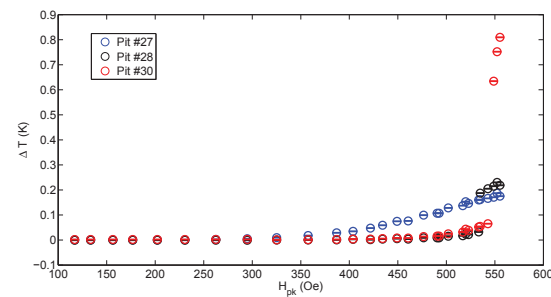


Figure 11: The heating of pit #27, #28 and #30 with radius $R = 750 \mu\text{m}$ versus surface magnetic field. The heating signals from pit #25, #26 and #29 are missing because of non-functional temperature sensors. The surface magnetic field on the horizontal axis is the peak surface field of the cavity, not taking into account the local field enhancement by the pits.

05 Cavity performance limiting mechanisms

F. Basic R&D bulk Nb - High performances

Fig. 8, 9, 10 and 11 show the measured heating signals from pits with radius $R = 200 \mu\text{m}$, $R = 300 \mu\text{m}$, $R = 600 \mu\text{m}$ and $R = 750 \mu\text{m}$ as function of the cavity field. Some of the pits heating data are missing because of non-functional temperature sensors. There are no effective heating signals from the six pits with the radius of $R = 400 \mu\text{m}$.

Most of the heating signals from the pits show a non-ohmic behavior at larger fields; refer to chapter 6.4 for a detailed discussion of this field dependence of the rf surface resistance. Importantly, it can be seen from Fig. 10 and 11 that the heating signals of pit #22 and #30 show a sudden jump to the $\sim 1 \text{ K}$ range at a cavity field at $\sim 545 \text{ Oe}$. These two pits eventually will cause a quench of the cavity at even higher field of 550 Oe.

The quench locations were found by measuring the length of time that the resistors stayed warm after the quench of the cavity [5]. The two pits # 22 and #30 were found to cause quench as shown in Fig. 12. Fig. 13 shows the heating versus magnetic field of the two quench pits #22 and #30. Assuming that the thermometer efficiency is about 25% [6], the inner side of cavity actually went up to 4 K just below quench. Both of the two pits show gradual heating until the temperature suddenly jumps to about $\sim 1 \text{ K}$ at a cavity maximum magnetic field around 545 Oe, which is smaller than cavity quench field of 550 Oe. Note that both pits are among the largest radius pits, which are expected to have the largest magnetic field enhancement [2].

What likely happened here for the two quench causing pits is that the local, enhanced field at pit edge reached the critical (superheating) magnetic field at given temperature, so part of the pit turned normal conducting. Thus the T-map sensors showed a sudden increase of temperature up to $\sim 1 \text{ K}$ and also the cavity quality factor Q_0 decreased significantly. The cavity did not quench at this field and did go to a bit higher in the field before quench occurred. So it is clear that the normal conducting edge of pit is initially stable until the field is too high. A ring-type defect model in chapter 6 will be presented to study this effect in more details.

Laser Confocal Microscopy Results

In order to obtain precise values of the pit edge radius r of the individual pits, silicone replicas were made to all thirty pits. The replicas were found to have at least $1 \mu\text{m}$ resolution. The replicas were then examined by laser confocal microscopy to measure the sharpness of the pit edges. Fig. 14 shows one of the images of a pit taken by laser confocal microscope. The dark area is the pit. In the bright area, the grain structure of the niobium surface can be seen very clearly.

Since the magnetic field is parallel to cavity equator, edges of pits perpendicular to the direction of the magnetic field show the highest fields due to magnetic field enhancement as shown in [2]. We only sample the pit edge curve profiles from those sections as indicated in Fig. 15. Fig. 16

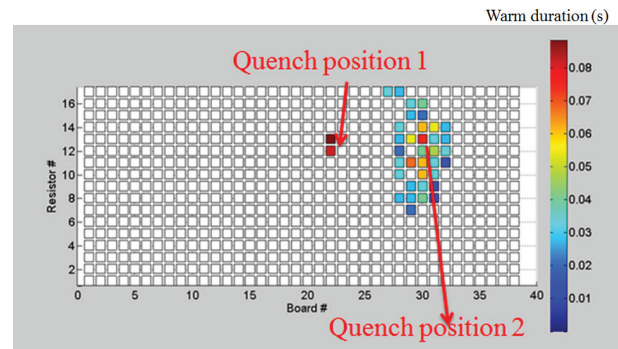


Figure 12: Quench locations of the pit cavity at a maximum surface magnetic field of $\sim 555 \text{ Oe}$. The quench locations were found by measuring the length of time that the resistors in the temperature map stayed warm after the quench of the cavity. The center of the quench location was found to be pits #22 and #30.

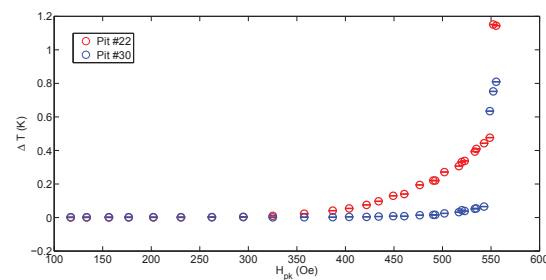


Figure 13: Heating of pit #22 and #30 versus the cavity maximum surface field H_{pk} . The uncertainty of measured field values is $\pm 10\%$. Notice the sudden jumps in ΔT at $\sim 540 \text{ Oe}$, corresponding to the sudden change in Q_0 at the same field; see Fig. 3. The surface magnetic field on the horizontal axis is the peak surface field of the cavity, not taking into account the local field enhancement by the pits.

shows a typical pit edge profile. The edge of the pit radius r is determined by the smallest curvature of the edge section of the profile. For every pit, 60 profile curves are taken from the 60 cross sections at different angles inside the magnetic field enhancement area of the pit. Then the range of pit edge radius r is measured from those 60 profile curves. Also the range of pit radius R is measured from those different pit profiles inside the magnetic field enhancement region. For example, Fig. 17 shows the distributions of r for three pits with the largest drill bit radius of $750 \mu\text{m}$. It can be seen that the pit #30 has the smallest average edge radius r around $10 \mu\text{m}$. Pit (28,6) and pit (28,12) have average edge radius of $30 \mu\text{m}$ and $24 \mu\text{m}$.

Table. 3 and 4 list the geometrical information measured by laser confocal microscopy including the range of pit radius R and the range of pit edge radius r for all 30 pits of 5 different drill sizes. The analysis of the resulting magnetic field enhancement at the pit is presented in the following chapter.

05 Cavity performance limiting mechanisms

F. Basic R&D bulk Nb - High performances

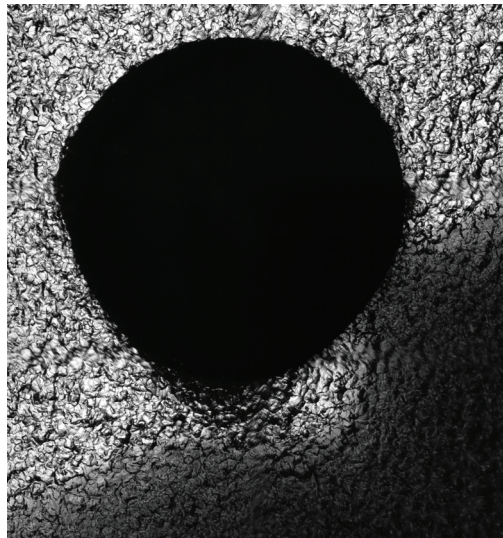


Figure 14: Image of pit #30 taken by laser confocal microscope. This pit is one of the pits causing the cavity to quench.

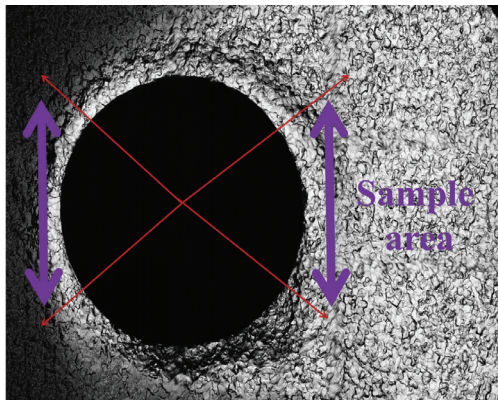


Figure 15: Area sampled for extracting edge profile data of the pits (Marked by double arrow).

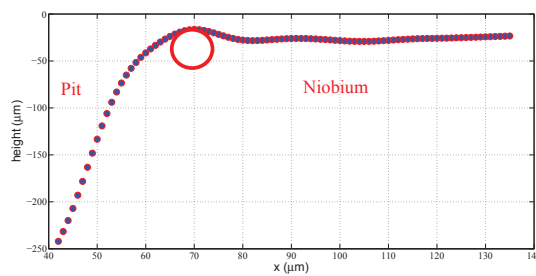


Figure 16: A typical pit edge curve extracted from the laser confocal microscopy image. The red circle is used to fit and obtain the edge radius r of the pit.

Table 3: The geometrical parameters of the artificial pits (I): the pits that have effective temperature readings measured by the T-map.

Pit number	Pit drill radius (μm)	Range of pit edge radius r (μm)	Range of pit radius R (μm)
#30	750	5~30	850~900
#27	750	20~55	880~900
#28	750	15~45	820~850
#23	600	30~60	520~550
#24	600	25~60	580~610
#22	600	5~45	570~610
#19	600	20~55	550~600
#20	600	35~60	570~600
#7	300	20~50	280~310
#6	200	25~55	180~210
#2	200	35~60	190~200

Table 4: The geometrical parameters of the artificial pits (II): the pits that do not have effective temperature readings measured by the T-map.

Pit number	Pit drill radius (μm)	Range of pit radius R (μm)	Range of pit edge radius r (μm)
#29	750	30~50	850~900
#26	750	10~45	850~870
#25	750	25~60	850~900
#21	600	25~60	600~650
#18	400	35~50	400~450
#17	400	20~35	350~400
#16	400	25~55	370~420
#15	400	20~50	400~450
#14	400	35~45	400~450
#13	400	25~40	400~420
#12	300	25~50	270~310
#11	300	20~50	290~320
#10	300	30~55	300~340
#9	300	35~60	280~320
#8	300	35~55	300~340
#5	200	20~45	200~210
#4	200	25~40	190~220
#3	200	25~50	200~220
#1	200	20~45	190~220

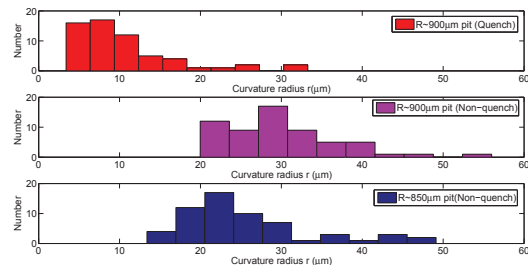


Figure 17: The distribution of edge radius r of three pits with nearly the same radius $750 \mu\text{m}$. The top one is pit #30. The middle one is pit #27 and the bottom one is pit #28.

NEW INSIGHTS INTO PITS BREAKDOWN AND HIGH FIELD Q-SLOPE

We will first introduce the magnetic field enhancement theory, which will be applied later to the pit cavity. A ring-type defect model will be then explained. Magnetic field enhancement calculations based on geometrical information of the pits inside the pit cavity will be presented and compared to the experimental results. Finally, observations of high field Q-slope based on the heating signal of the pits will be discussed.

Magnetic Field Enhancement at the Edge of a Pit

The magnetic field enhancement effect at the sharp edge/corner of a pit as shown in Fig. 18 has been calculated in previous work [2, 7, 8]. The results obtained for sufficiently deep pits ($\text{depth} > R$) generally show that the magnetic field enhancement factor β can be expressed as [2]

$$\beta = C \left(\frac{r}{R} \right)^{-1/3}, \quad (2)$$

where r is the radius of edge/corner, R the radius of the pit, and C is a constant of about 1.17. Accordingly, pits with larger radius or sharper edges cause a larger magnetic field enhancement.

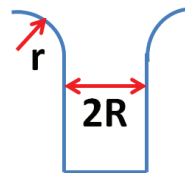


Figure 18: The sketch of a pit with radius R and edge radius r .

Real pit-like defects observed in the superconducting cavities have a complex 3-dimensional shape. To obtain a realistic field enhancement factor for these pits, I used SLAC's parallel computing EM code ACE3P [9] to compute the exact surface magnetic field in the entire pit edge area. Studies have shown that Omega3P has a very accurate

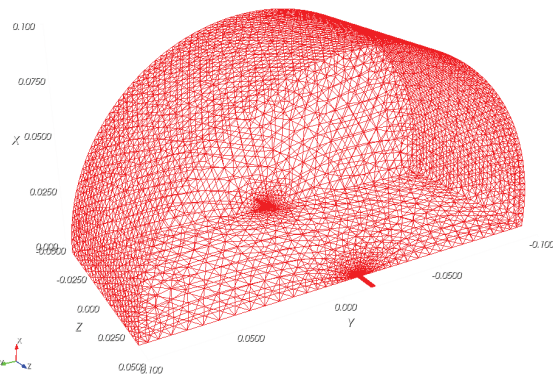


Figure 19: Geometry and mesh configuration used for the 3D pit magnetic field enhancement calculations.

surface field precision compared to other 3-dimensional codes. As a first, simple example, we have simulated a rounded pit on the axis of a pillbox cavity with the TE₁₁₁ mode. The size of the modeled pit is small compared to the size of the cavity, which ensures that the surface field would be uniform over the area of the pit without the pit present. The pillbox cavity has a radius 100 mm, with a pit radius $R = 1 \text{ mm}$. The simulated geometry and mesh configuration can be seen in Fig. 19 and Fig. 20.

The calculation was performed and checked with different mesh densities. As the pit edge radius r becomes smaller, the surface field calculated by Omega3P becomes more dependent on the mesh densities. Nevertheless, for sufficiently dense meshes, our calculated results agree well with the $(r/R)^{-1/3}$ dependence of the maximum surface enhanced magnetic field as shown in Fig. 22. An example of the calculated surface magnetic field distribution is shown in Fig. 21. The corresponding field enhancement factor near the edge of the pit is displayed in Fig. 23. An angular non-uniform field enhancement around the edge can be seen from these results, with significant field enhancement in some sections. The maximum magnetic field

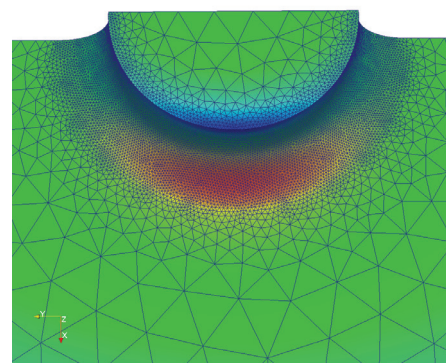


Figure 20: Mesh configuration at the pit used for 3D magnetic field enhancement calculations. Here $R = 1 \text{ mm}$, $r = 75 \mu\text{m}$.

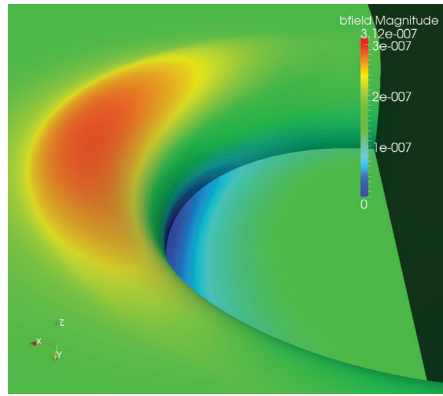


Figure 21: Magnetic field distribution near the pit edge. The direction of the magnetic field is in the x-direction outside of the pit.

enhancement factor is about 2.65 which is in good agreement with the calculation results using Eqn. 2.

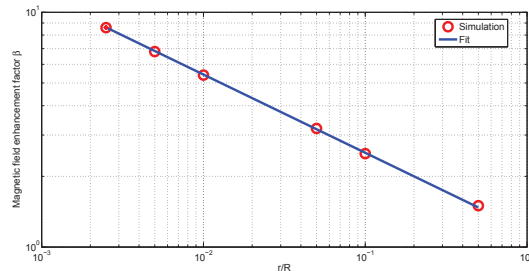


Figure 22: Magnetic field enhancement factor calculation by ACE3P using a 3-d model. The fit equation is $\beta = 1.17 * (r/R)^{-1/3}$.

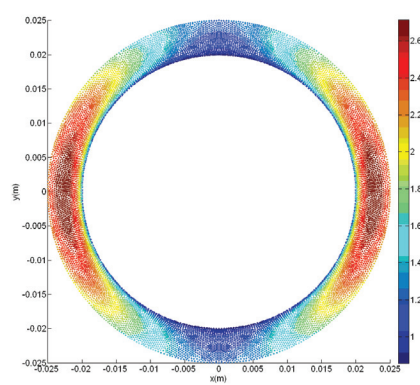


Figure 23: Magnetic field enhancement near the pit edge.

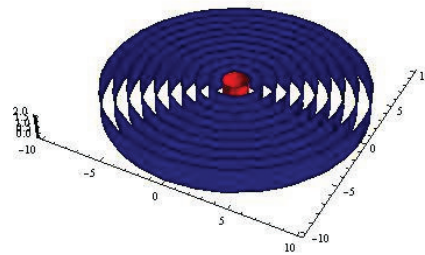
Ring-type Defect Model Based on Magnetic Field Enhancement on Ring Edges

The phenomena of thermal magnetic breakdown has been numerically simulated over the years and is based on a

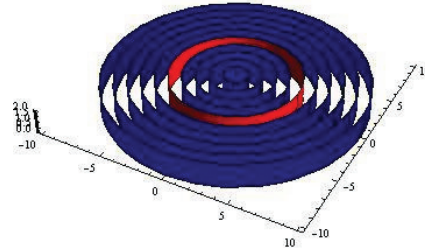
05 Cavity performance limiting mechanisms

F. Basic R&D bulk Nb - High performances

thermal feedback process. Past models treated the defect as an axial-symmetric disk with its entire area becoming normal conducting when thermal breakdown happens. However, as observed in many cases, quench causing defects are correlated with pits on the surface with a sharp edge, and not disk like objects. Therefore, based on the assumption that only the edge of the pit becomes normal conducting, a 2-dimensional ring-type defect thermal program was developed. Figure. 24 shows the mesh configuration difference between a ring-type defect and a disk-type defect. The ring-type defect model is based on the same heat balance equations and boundary conditions as the disk-defect thermal model [10].



(a) Mesh configuration for a disk-type defect



(b) Mesh configuration for a ring-type defect

Figure 24: Different mesh distributions of ring type and disk type defect models with normal conducting (red) and superconducting (blue) mesh elements.

In the ring-type defect model, the program splits a cylindrical section of the niobium wall into many circular ring-shaped mesh elements. To model the heating at the edge of the pit, in the first version of the ring defect model a normal conducting defect was located at a ring section at a certain distance from the center of the modeled niobium disk. To speed up simulations, the mesh density is higher near the defect element and lower away from it, where temperature gradients are smaller. The mesh spacing in the radial direction was chosen to increase exponentially (the distance between the i -th element to the ring-defect is proportional to e^i). The z direction (through the niobium) can also be easily meshed using an exponential function. For a selected surface field at one side of the niobium disc, the rf power is calculated based on the temperature dependent surface resistance. Given the temperature dependent thermal conductivity of niobium and Kapitza conductance between niobium and helium, the rf power produced at the surface is

compared with the power emitted into the helium bath at a given iteration number. The over-relaxation method [11] is used to estimate the $(n + 1)$ -th iteration from the n -th iteration. Once the two heat transfer numbers are sufficiently equal (e.g. their difference is less than 1.0×10^{-6}), thermal equilibrium is reached and a valid solution is found.

In the second, improved version of the ring defect model, a position dependent magnetic field enhancement (MFE) factor at the rf surface is added to better mirror the situation found in pit defects. For a first approximation, the enhancement factor is one far outside of the pit and jumps to a selected value above one at the pit edge of a given width. Inside the pit, the field enhancement factor is scaled below one because the surface magnetic field inside the pit is lower compared to the field at the flat surface outside of a pit.

Accordingly, the radius of the "ring defect" in the model is equal to the radius R of the pit, and the width of the "defect" is assumed to be equal to the radius r of the edge of the pit, where the MFE factor is high. Initially in the model, the entire surface is assumed to be superconducting. Only when the field exceeds the superheating (critical) magnetic field at the given temperature of the niobium at a given location, that section of the surface is assumed to become normal conducting. Since an axis-symmetric mesh is used, a uniform MFE factor is assumed instead of angular dependent MFE factor along the pit edge. Nevertheless, a 3-dimensional electromagnetic code is used to obtain realistic magnetic field enhancement factors based on measured surface pit dimensions.

Simulations of pit defects of different radius R and edge width r (and thus different field enhancement factor at the pit) were performed to explore the relationship between the pit geometry and the quench field. Fig. 25 shows the temperature profile on the rf surface as function of radial distance from the center of the pit at a field just below quench. Clearly visible is the heating by the edge of the pit becoming normal conducting. The normal conducting resistance of niobium was taken as $10 \text{ m}\Omega$. Future versions of the ring defect model will also take into account the temperature dependence of the normal conducting resistance.

Fig. 26 shows a typical pre-quench temperature distribution at the cross section of the simulated heating by a pit. The rf field level (enhanced field at the edge of the pit) is 1315 Oe which is slightly below the quench field of this pit defect of 1319 Oe. As can be seen from Fig. 26, the highest temperature located at the pit edge is 5.76 K. In contrast, the critical temperature of niobium at this field level (enhanced field at the edge of the pit) is 5.4 K. This confirms that the pit edge has become normal conducting, while inside the pit the niobium remains superconducting. As the field increases further, the normal conducting pit edge expands and finally leads to a thermal instability (quench), when the entire simulated niobium slab becomes normal conducting.

In conclusion, the ring-type defect pit model with magnetic field enhancement at the pit edge predicts that the

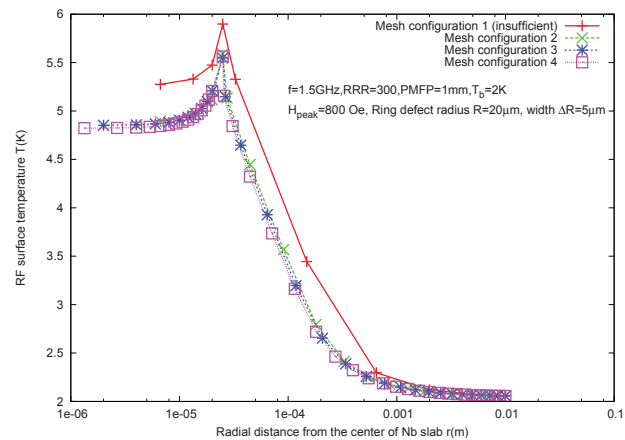


Figure 25: RF surface temperature distribution along the radial direction for a given ring-type defect with $R = 20 \mu\text{m}$ and $r = 5 \mu\text{m}$. The rf frequency is 1.5 GHz, RRR = 300, phonon mean free path = 1 mm, bath temperature = 2 K, magnetic field = 800 Oe and the normal conducting defect resistance is $10 \text{ m}\Omega$.

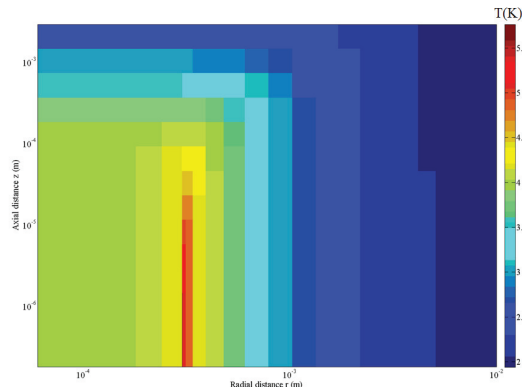


Figure 26: Temperature distribution in Kelvin over the cross section of the simulated niobium slab at a field level of 1315 Oe (enhanced field at the edge of the pit) which is slightly below the quench field of this pit defect of 1319 Oe. The diameter of the simulated niobium disk is 10 mm with 3 mm thickness. The field enhancement factor used at the edge of the pit corresponds to a pit of $R = 30 \mu\text{m}$ diameter with a edge radius r of $1 \mu\text{m}$. The helium bath temperature is 2 K. The rf surface in the image is at the bottom, and the side facing the helium is at the top.

edge first gets normal conducting, but remains thermally stable, and then at a somewhat higher field (about a few percent), the whole cavity quench happens. The temperature map data for the sensors on top of the pits causing quench in the pit cavity shows the same: first a step in ΔT when the edge becomes normal conducting, and then the cavity quench at a slightly higher field as shown in Fig. 13.

05 Cavity performance limiting mechanisms

F. Basic R&D bulk Nb - High performances

Table 5: The magnetic field enhancement calculation results based on the geometrical parameters of the artificial pits (I): the pits that have effective temperature readings measured by the T-map.

Pit number	Pit drill radius (μm)	Range of pit edge radius r (μm)	Range of pit radius R (μm)	Range of magnetic field enhancement factor $\beta = 1.17 * (r/R)^{-1/3}$	Range of local magnetic fields at H_{pk} reached in the pit cavity (Oe)
#30	750	5~30	850~900	3.6~6.6	1940~3560
#27	750	20~55	800~850	2.9~4.1	1560~2210
#28	750	15~45	790~810	3.0~4.4	1620~2370
#23	600	30~60	520~550	2.4~3.1	1290~1670
#24	600	25~60	580~610	2.5~3.4	1350~1830
#22	600	5~45	570~610	2.7~5.8	1460~3130
#19	600	20~55	550~600	2.5~3.6	1350~1940
#20	600	35~60	570~600	2.5~3.0	1350~1620
#7	300	20~50	280~310	2.1~2.9	1130~1560
#6	200	25~55	180~210	1.7~2.4	910~1290
#2	200	35~60	190~200	1.7~2.1	910~1130

Analysis of Magnetic Field Enhancement in the Pit Cavity

By applying the magnetic field enhancement theory to the measured shape data of the pits in the pit cavity, the range of field enhancement factors and the range of local fields at the pit edges at the highest field achieved in the pit cavity (~ 555 Oe) can be calculated, as is summarized in Table. 5. Here local magnetic field at the pit edge $H_{local} = 0.98 * H_{pk,cavity} * \beta$.

The superheating field at 1.6 K is $1900 \sim 2300$ Oe, depending on the purity of the niobium. From Table. 5, it can be seen that pit #30, #28, #27 and #22 are predicted to transition first to the normal conducting state at cavity fields near the measured quench field, since the local magnetic field is above the critical field. Indeed, the heating signals from pit #30 (see Fig. 27), #28 (see Fig. 28), #22 (see Fig. 29) measured by the T-map showed a clear jump in ΔT , i.e. a transition of the edge to the normal conducting state.

Fig. 30 shows the heating measured by T-map sensors versus magnetic field at the position of the pit #27. The maximum heating is about 200 mK when the cavity quenches. It does not have a clear jump compared to pit #30 and #28 of the same drill bit radius. It may be the case because the pit has a lower local magnetic field at the pit edge compared to pit #30 and #28, as shown in Table. 5. Fig. 31 shows the laser confocal images of pit #30, #28 and #27. It can be seen that there are some visible differences among the pit edge radii of the three pits. Pit #30 and #28 have sharper edges, and #27 does not.

The MFE model correctly predicts which pits have the largest MFE and thus should become normal conducting first, and ultimately will limit the performance of the cavity by causing it to quench. It also correctly predicts the approximate field at which that should happen. This shows that the pits found in srf cavities can cause quench and thus

05 Cavity performance limiting mechanisms

F. Basic R&D bulk Nb - High performances

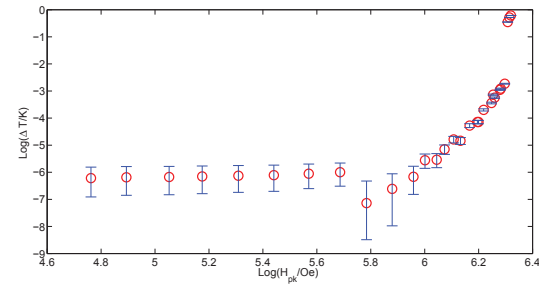


Figure 27: Heating measured by the temperature mapping sensor versus magnetic field at the position of the pit #30. The data is plotted on a log scale. The surface magnetic field on the horizontal axis is the peak surface field of the cavity, not taking into account the local field enhancement by the pits.

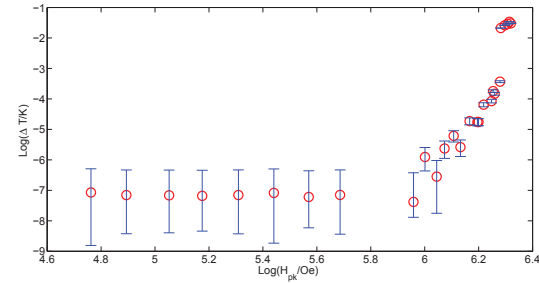


Figure 28: Heating measured by the temperature mapping sensor versus magnetic field at the position of the pit #28. The data is plotted on a log scale. The surface magnetic field on the horizontal axis is the peak surface field of the cavity, not taking into account the local field enhancement by the pits.

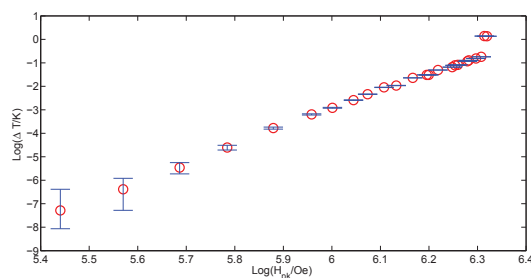


Figure 29: Heating measured by the temperature mapping sensor versus magnetic field at the position of the pit #22. The data is plotted on a log scale. The surface magnetic field on the horizontal axis is the peak surface field of the cavity, not taking into account the local field enhancement by the pits.

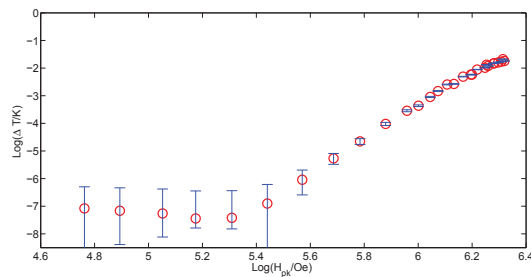
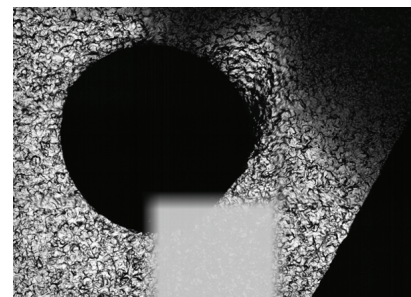


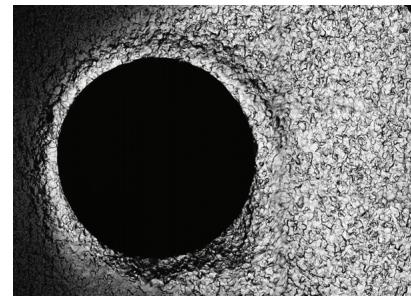
Figure 30: Heating measured by the temperature mapping sensor versus magnetic field at the position of the pit #27. The data is plotted on a log scale. The surface magnetic field on the horizontal axis is the peak surface field of the cavity, not taking into account the local field enhancement by the pits.



(a) Pit #30



(b) Pit #28



(c) Pit #27

Figure 31: Laser confocal microscopy picture of three pits #30 (top), pits #28 (middle) and pits #27 (bottom).

limit the performance of the cavity only if their edge radius is a few μm and if they are in the high magnetic field region. This also explains why some pits are a problem and others are not.

Analysis of High Field Behavior of the Superconducting Pit Edges

In addition to the two quench causing pits verified by T-map sensors, there are 9 pits that do not cause quench, but still showed measurable heating signals. Assuming there is magnetic field enhancement at these pit edges, the temperature rise information versus real local magnetic field can provide new valuable information about the high field Q-slope.

At low fields, assuming that the surface resistance is field independent, one expects the heating signal will be proportional to H^2 . Fig. 32 shows the heating versus magnetic field for pit #2 and #6. It clearly shows an ohmic behavior due to a field-independent BCS surface resistance.

Fig. 33 shows the heating signals versus magnetic field of pit #22 and #19. For pit #19, below field level of $\log(H_{pk}/\text{Oe}) < 4.6$, the pit heating signal is so small

that it is below noise level. Within the field range of $5.6 < \log(H_{pk}/\text{Oe}) < 6.2$, the heating signal obeys a power law with an exponent of 8. Above field level of $\log(H_{pk}/\text{Oe}) > 6.2$, the heating signal does not show an abrupt jump as those pits that induce cavity quench but rather increases more slowly with a power law of an exponent of 4. The maximum heating is about 450 mK when the cavity quenches.

Fig. 34 and 35 shows the heating signals versus magnetic field of pit #24, #23 and #7. The heating signals also can be clearly divided into three sections as described previously for the case of pit #19, shown in Fig. 33(b).

The slope information from the pit heating is summarized in Tab. 6, taking into account the local magnetic field enhancement factors as given in Table. 5.

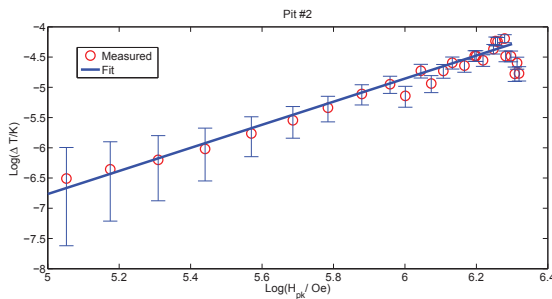
The following observations can be made based on the slope of the pit heating signals.

05 Cavity performance limiting mechanisms

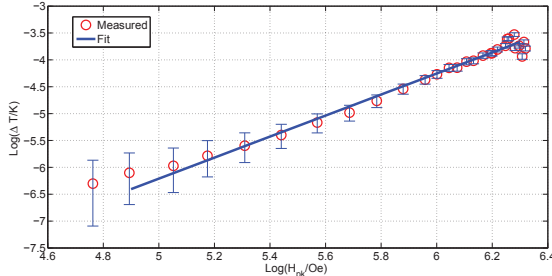
F. Basic R&D bulk Nb - High performances

Table 6: Slope information from fitting the field dependence of the heating signals of the pits (Only for pits that do not cause quench).

Pit number	Slope of $\ln(\Delta T/K)$ vs $\ln(H_{pk}/Oe)$ in field region I ($H_{local} < 800$ Oe)	Slope of $\ln(\Delta T/K)$ vs $\ln(H_{pk}/Oe)$ in field region II (800 Oe $< H_{local} < 1300$ Oe)	Slope of $\ln(\Delta T/K)$ vs $\ln(H_{pk}/Oe)$ in field region III ($H_{local} > 1300$ Oe)
#27	~ 2	6.2	4.3
#28	~ 2	10.0	5.0
#23	~ 2	8.3	4.2
#24	~ 2	8.4	4.8
#19	~ 2	7.8	4.1
#20	~ 2	8.1	4.6
#7	~ 2	8.5	4.0
#6	1.92	N/A	N/A
#2	1.97	N/A	N/A



(a) Pit #2



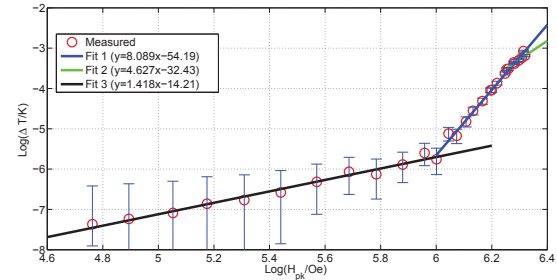
(b) Pit #6

Figure 32: Measured heating signals versus magnetic field for pit #2 (top) and #6 (bottom) with the smallest drill bit radius of 200 μm . Both fit has a slope of 2 in the log-log graph, i.e., the heating is proportional to H^2 . The surface magnetic field on the horizontal axis is the peak surface field of the cavity, not taking into account the local field enhancement by the pits.

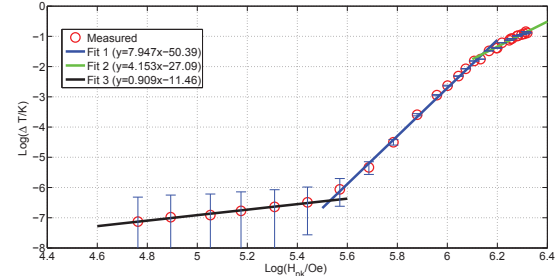
- At low field, the heating is proportional to H^2 , as one would expect for ohmic heating;
- At higher fields, there is clear transition to a strong non-linear behavior, with a final slope of $\log(\Delta T/K)$ versus $\log(H_{pk}/Oe)$ of 4 to 5 at highest fields. This points to a strong field dependence of the BCS surface resistance, for local fields in the 1000 \sim 2000 Oe region at the edges of the pits. It should be noted

05 Cavity performance limiting mechanisms

F. Basic R&D bulk Nb - High performances



(a) Pit #20



(b) Pit #19

Figure 33: Measured heating signals versus magnetic field for pit #22 (top) and #19 (bottom) with a drill bit radius of 600 μm . The surface magnetic field on the horizontal axis is the peak surface field of the cavity, not taking into account the local field enhancement by the pits.

here that the situation is rather complex, since only a small area at the pit edge is at high fields, and it is not uniform. Nevertheless, from the slope information one concludes that the BCS surface resistance scale with the magnetic field to a power of 4 to 6 at medium fields, and with a power of ~ 2 of the high fields above 1300 Oe.

- The transition to field dependent surface resistance happens at fields similar to where the high field Q-

slope starts in BCP cavities (~ 900 Oe), taking into account the MFE at the pit edges;

- The pit heating data shows that a BCS cavity surface can reach high fields close to the superheating field. The strong Q-slope found in BCS cavities above ~ 900 Oe thus is likely caused by a combination of a non-linearity of the BCS surface resistance and thermal feedback caused by the increased rf losses over a larger area. For the pit edges, the high field area is very small, so the total power disposed is small and

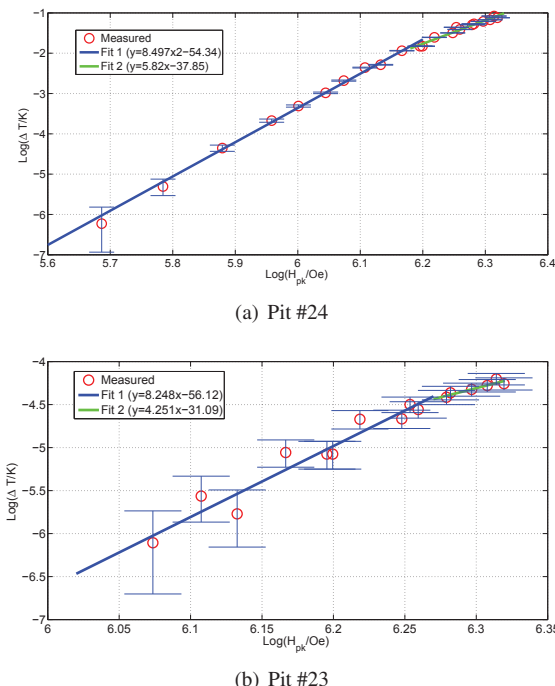


Figure 34: Measured heating signal versus magnetic field for pit #24 (top) and #23 (bottom) with a drill bit radius of $600 \mu\text{m}$. The surface magnetic field on the horizontal axis is the peak surface field of the cavity, not taking into account the local field enhancement by the pits.

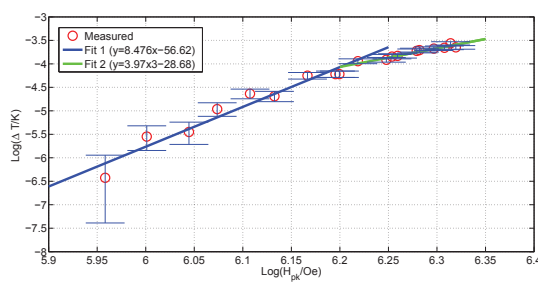


Figure 35: Measured heating signal versus magnetic field for pit #7 with a drill bit radius of $300 \mu\text{m}$. The surface magnetic field on the horizontal axis is the peak surface field of the cavity, not taking into account the local field enhancement by the pits.

thermal feedback is less important.

These results will be useful to guide future theoretical work on understanding the field dependence of the surface resistance.

CONCLUSIONS

The small pits often found on the inner surface of srf cavities are frequently limiting the maximum field gradient in these cavities. However not all pits present a problem to cavity performance. So it is very desirable to study those pits systematically to determine the related parameters. I have made a single cell cavity with 30 artificial pits in the high magnetic field region to gain new insight in how pits limit the cavity performance. The relevant parameters are the pit diameter, the pit edge radius and the pit height. The test of the pit cavity showed clear evidence that the edges of two of the largest radius pits transitioned into the normal conducting state at a field just below the quench field of the cavity, and that the quench was indeed induced by these two pits. I also measured the shape of the 30 pits by laser confocal microscopy. Predictions by a magnetic field enhancement factor $\beta \sim (r/R)^{-1/3}$ model which depends on the radius of the pits R and the radius of the edge of the pits r is in good agreement with the observed behavior of the artificial pits in the cavity. I also developed a ring-type defect model which gives further insight into the heating and quench behavior of pits. The pits also give some new insight into the non-linear surface resistance of niobium at high fields.

ACKNOWLEDGEMENT

We thank Hasan Padamsee and Valery Shemelin for discussions and suggestions about drilled pits and magnetic field enhancement effect. We thank Dan Gonnella for helping on pits cavity rf tests, Sam Posen for helping on T-mapping and Mingqi Ge for laser confocal microscopy measurement. This work was supported by by NSF CAREER award PHY-0841213 and A. P. Sloan Foundation.

REFERENCES

- [1] Y. Xie, Hasan Padamsee, Alexander Romanenko, “Relationship Between Defects Pre-Heating and Defects Size”, SRF2009, Berlin, Germany.
- [2] V. Shemelin, H. Padamsee, “Magnetic field enhancement at pits and bumps on the surface of superconducting cavities”, SRF Report 080903-04, Cornell University.
- [3] Y. Xie, M. Liepe, H. Padamsee, “Thermal modelling of ring-type defects”, SRF2009, Berlin, Germany.
- [4] D. Myakishev and V. Yakovlev, “The new possibilities of SuperLANS code for evolution of axisymmetric cavities”, PAC95, Texas, USA.
- [5] D. Gonnella et. al., “QUENCH STUDIES OF A SUPERDUCTING RF CAVITY”. IPAC12, New Orleans, USA, 2012.
- [6] J. Knobloch, et.al., “High field Q-slope in superconducting cavities due to magnetic field enhancement”, SRF99, Santa Fe, New Mexico.

05 Cavity performance limiting mechanisms

F. Basic R&D bulk Nb - High performances

- [7] J. Knobloch, PhD thesis, Cornell University, 1997.
- [8] Y. Iwashita, “*Evaluation of Magnetic Field Enhancement Along a Boundary*”, Linac04, Lubeck, Germany.
- [9] Lie-Quan Lee, Zenghai Li, Cho Ng, and Kwok Ko, Tech. Rep., SLAC-PUB-13529, 2009, “*Omega3P: A Parallel finite-Element Eigenmode Analysis Code for Accelerator Cavities*”.
- [10] J. Vines, et.al., “*Systemtic trends for the medium-field Q-slope*”, SRF07, Beijing, China.
- [11] Richard S. Varga, Matrix Iterative Analysis, Second ed., Springer-Verlag, 2002.